DISCLAIMER

This report was prepared as an account of work sponsored by an agency of the United States Government. Neither the United States Government nor any agency thereof, nor any of their employees, makes any warranty, express or implied, or assumes any legal liability or responsibility for the accuracy, completeness, or usefulness of any information, apparatus, product, or process disclosed, or represents that its use would not infringe privately owned rights. Reference herein to any specific commercial product, process, or service by trade name, trademark, manufacturer, or otherwise does not necessarily constitute or imply its endorsement, recommendation, or favoring by the United States Government or any agency thereof. The views and opinions of authors expressed herein do not necessarily state or reflect those of the United States Government or any agency thereof. Reference herein to any social initiative (including but not limited to Diversity, Equity, and Inclusion (DEI); Community Benefits Plans (CBP); Justice 40; etc.) is made by the Author independent of any current requirement by the United States Government and does not constitute or imply endorsement, recommendation, or support by the United States Government or any agency thereof.

NEW MEXICO INSTITUTE OF MINING AND TECHNOLOGY

SOCORRO, NEW MEXICO

Final Report on

Dissimilar metal joining of Ti-6Al-4V and Inconel 625

BY

Ethan Hopwood
Annika Bauman

TO

DEPARTMENT OF MATERIALS AND METALLURGICAL ENGINEERING
May 9th, 2025

1 Abstract

The dissimilar joining of Ti-6Al-4V and Inconel 625 by using a suitable interlayer shows potential design flexibility by avoiding the brittle intermetallic phases from direct welding. These phases include $NiTi$, $NiTi_2$, and Ni_3Ti. The objective of this work is to facilitate laser welding of Ti-6Al-4V and Inconel 625 through a vanadium interlayer to form an intermetallic free, strong, and corrosion resistant joint. Vanadium was chosen based on binary phase diagram solubilities, literature, and theoretical CalPhaD calculations in PanDat. Laser welding was systematically explored from based on beam mode, offset, power, and scan speed. Varied parameters include laser power from 325 to 650 watts, laser scan speed from 80 to 160 in/min, and beam offset up to a $\frac{1}{4}$ of the beam diameter. Parameters were chosen based on previous dissimilar joining research and those found in the literature. Metallography, including optical and scanning electron microscopy, was used to analyze the weld chemical composition, grain structure, and defects through both the fusion and heat affected zones. The results and discussion will examine the relationship between process parameters, microstructure, and observed weld defects. Our findings will not only assess the weldability of vanadium and Inconel 625 but also establish a transferable framework for studying other dissimilar material combinations, providing valuable insights for future research in this field.

2 Graphical Abstract

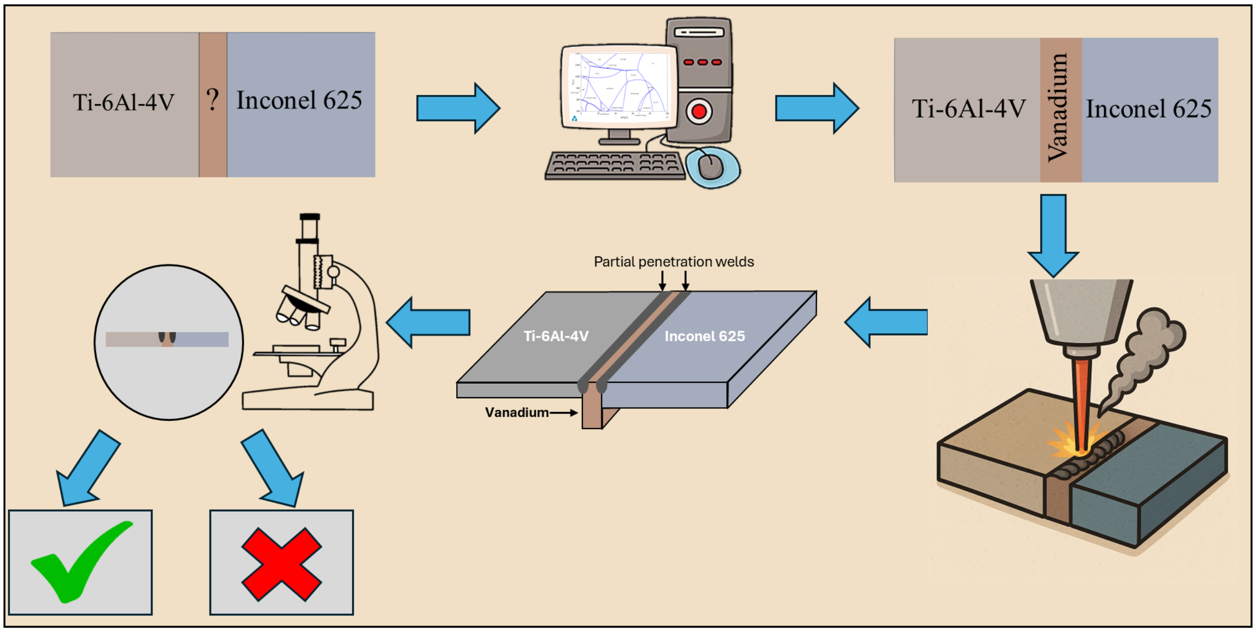

Figure 1: Graphical abstract

3 Introduction

Industries constantly need lighter and stronger materials for a wide variety of applications. In order to achieve this, multi-material use is necessary and dissimilar joining may be a viable option. Dissimilar joining is beneficial for manufacturing through its weight reduction and increase in performance.[1] Laser welding is one method for dissimilar joining that has increased in popularity because of it's low heat input per unit length and efficiency. For example, welding $\frac{1}{2}$ inch thick material with laser welding is 15-20 times faster than Metal Inert Gas (MIG) welding.[2] Laser beam welding (LBW) is a high energy density (HED) process that focuses the necessary energy to melt the metal into a very fine beam. This results in a weld mode referred to as keyhole welding where the weld is narrow and deep. Lowering the power or expanding the beam spot size can result in a different mode referred to as conduction welding where the resulting weld is shallow and wide. This difference is illustrated in Figure 2.

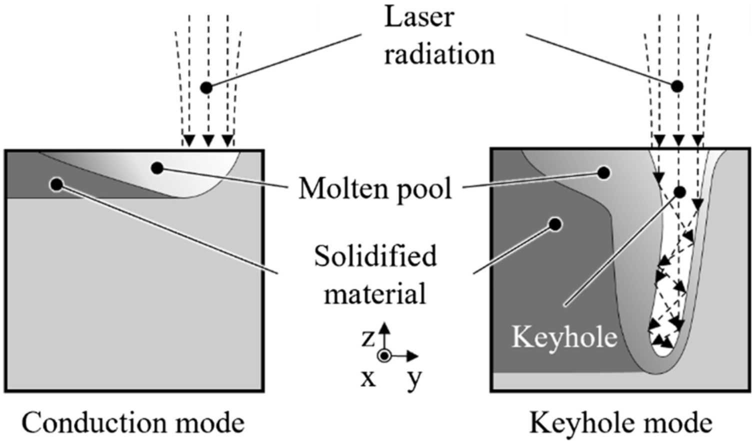

Figure 2: Conduction versus keyhole mode welding[3]

Energy densities can approach and exceed $10^4 \left(\frac{kW}{cm^2}\right)$ whereas arc welding processes are in the 0.5-50 $\left(\frac{kW}{cm^2}\right)$ range.[4] It is not uncommon in the arc welding industry to manipulate the weld pool to better tie in work pieces being joined. The same is available for laser welding and is referred to as beam oscillation or wobble welding. The beam travels in a specified path such as a circle as it also travels along the joint. The frequency of oscillations and amplitude of the path is defined in the programming software. A laser weld that travels straight down the joint without any oscillation is referred to as continuous wave welding. The differences are shown in Figure 3 and 4. Laser welding is commonly used as an autogenous process where no filler metal is added to the melt pool.

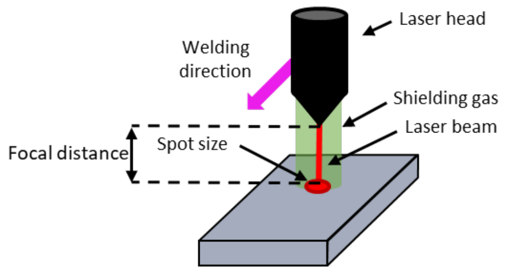

Figure 3: Continuous wave schematic

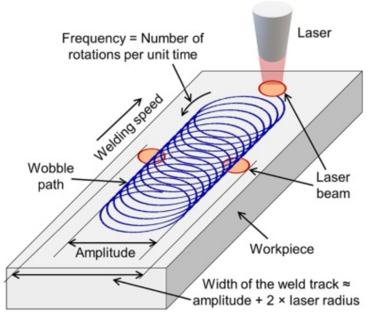

Figure 4: Beam oscillation schematic[6]

Ti-6Al-4V and Inconel 625 were selected to join through an interlayer because of their corrosion resistance, high strength, and titanium's low density. Ti-6Al-4V has a high specific strength that is desirable in a multitude of applications, and Inconel 625 has high creep and corrosion resistance in aggressive environments such seawater. Combined these two are useful in high strength and corrosion based applications such as marine environments where galvanic corrosion is important to consider[20] This weld combination would also be useful in power generation for coolant systems and control rod drive components.[1,8]

Because they are dissimilar, Ti-6Al-4V and Inconel 625 are not easily joined together. Namely, they form brittle intermetallic compounds (IMC) that weaken the strength of the joint; these include $NiTi, Ti_2Ni, TiNi_3$. The phase diagram of nickel and titanium is shown in Figure 5. They also have different thermophysical properties shown in Table 1. Titanium is also a highly reactive metal with oxygen and hydrogen which can weaken the weld further.[9] Due to these reasons finding a suitable interlayer to place between them would be a viable option for joining.

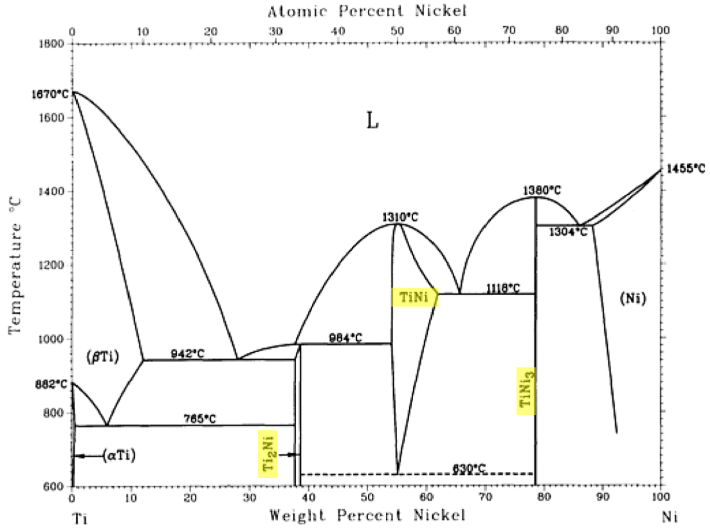

Figure 5: Ti-Ni phase diagram with intermetallics highlighted [J.L. Murray, 1991]

In literature, vanadium has been investigated as an interlayer. W. Wang, et all have successfully used a vanadium interlayer through laser melting deposition (LMD) to combine Ti-6Al-4V and Inconel 625.[10] LMD differs from laser welding through the types of material.

LMD utilizes powder to weld the two together where as laser welding melts each metal sheet together and fuses upon cooling. Wang previously used a diffusion bonded vanadium and copper interlayer through LMD. There has been more extensive literature with Ti-6Al-4V and Inconel 718 as a combination. Scientists have used niobium, vanadium, molybdenum, and copper with varying degrees of success.[11,12,13] Inconel 718 has about 20% iron in its composition which can complicate the interlayer choice. Because there has been some successful interlayers with a more complex composition of Inconel, it could translate to Inconel 625 which has a low iron composition.

Laser welding Inconel alloys and Titanium alloys use widely different parameters. There are many different datasets in the literature for both, but it also machine specific. CO_2 gas laser versus Nd:YAG laser can change power, scan speed, gas flow, and spot size values. For Titanium alloys, Sandia National Laboratories has found a parameter set that works well with the vanadium interlayer after multiple rounds of testing. But in a quick literature review, E. Akman et. all did a study with a pulsed Nd:YAG laser and found that the high power with a shorter pulse made a deeper weld.[16]

Table 1: Relevant thermophysical properties [matweb]

Property	Ti-6Al-4V	Inconel 625	Vanadium
Coefficient of thermal expansion $\left(\frac{\mu m}{m * ^\circ C}\right)$	9.7	12.8	8.33
Thermal conductivity $\left(\frac{W}{m * K}\right)$	6.7	9.8	31
Melting temperature (°C)	1604-1660	1290-1350	1735
Specific heat capacity $\left(\frac{J}{g \cdot ^\circ C}\right)$	0.53	0.41	0.50

Currently, Lin Yan et. all tested some parameters for a Nd:YAG laser welder where they changed the laser power from 300-400 watts and the scan speeds to find the most ideal parameter set.[14] This information will be useful for testing and seeing what can be replicated with our system. Fidel Zapirain et. all used both a CO2 laser and Nd:YAG laser to butt weld together Inconel 625 and Inconel 718.[20],[15] They had good welds, but did not disclose what their parameters were for both the CO2 and Nd:YAG lasers. Hui Chi Chen et al. experimented with the direct laser welding of Inconel 718 and Ti-6Al-4V through fiber laser welding and found that intermetallic free joints could be formed through power, offset, and scan speed optimization[18].

The novelty of this work is joining Inconel 625 and Ti-6Al-4V with only a single vanadium interlayer through laser welding.

4 Methods

4.1 Theoretical

Binary phase diagrams were initially explored for elements that are readily soluble in either titanium or nickel because they are the largest constituents of the two alloys. BCC structured refractory metals such as niobium, molybdenum, and vanadium are fully soluble in titanium, but have limited solubility in nickel. An FCC-structured material such as copper is fully soluble in nickel but has almost no solubility in titanium. Vanadium satisfied this condition the best of all metals examined with a solubility in nickel of roughly 40% at 1200°C.

PanDat, a software that uses the CALPHAD method, was used to generate equilibrium phase diagrams between the bulk Inconel 625 composition seen in Table 13 in Appendix A, and the three pure refractory metals. The diagrams for niobium and molybdenum can be seen in Appendix A which show significant amounts of topologically close packed (TCP) structures such as P, μ, and Laves phases. The generated phase diagram for vanadium and Inconel 625 can be seen in Figure 8. Welding is inherently a non-equilibrium process so Scheil solidification diagrams were also calculated using PanDat. The diagram showing a composition of 50 wt% Inconel 625 and 50 wt% vanadium is shown in Figure 9.

4.2 Fabrication

4.2.1 Materials

Commercially available vanadium, Ti-6Al-4V, and Inconel 625 were cut and machined to the sizes specified in Table 2. Sample faces to be welded were dressed to remove burrs and create a square surface before welding to ensure proper fit-up. Samples were also cleaned with acetone and isopropanol to remove machining grease.

Table 2: Material measurements

Material	Inconel 625	Ti-6Al-4V	Vanadium
Length (in)	2	1	1
Width (in)	1	1	0.125
Thickness (in)	0.125	0.0625	0.25

4.2.2 Welding Equipment and Parameters

Since the materials varied in thickness they were placed face down on a fixture plate and clamped together in a butt joint as seen in Figure 6 before being tack welded in a flash-lamp LaserStar welder. The tacked specimens were then removed from the fixture plate and flipped so the flat face was pointed upwards. 304L stainless steel plates were then used to raise up both sides of the joint so the vanadium interlayer was held above the fixture plate. Both sides of the joint were then clamped down to the 304L to hold the material in place for welding. The focus of the beam was set to the top of the samples to be welded. A macro image of a completed joint is shown in Figure 7.

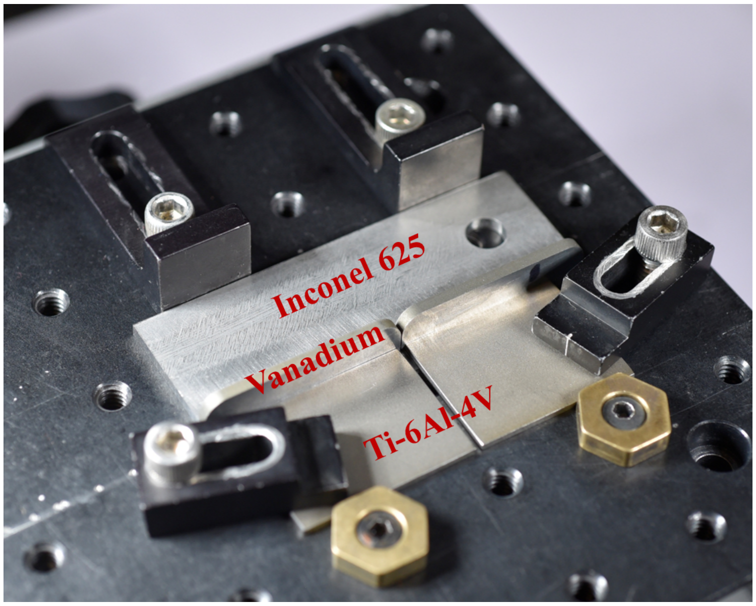

Figure 6: Sample fixturing

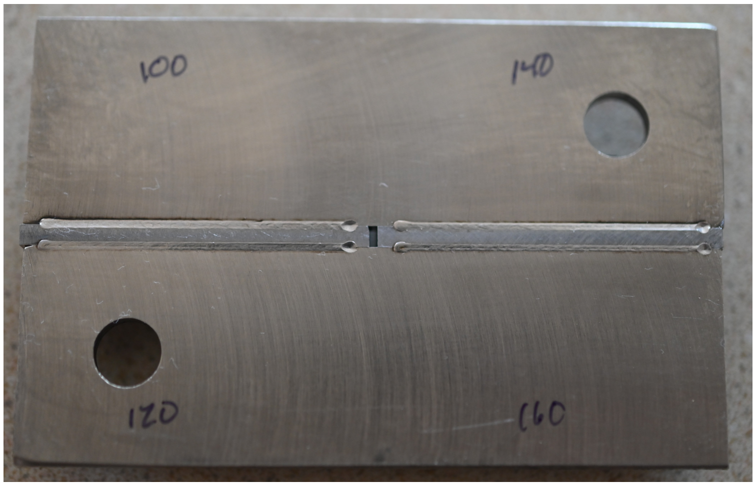

Figure 7: Macro image of completed joint

Laser welding was done in two separate machines; continuous wave welds were done in a Mundt 2kW Fiber Laser and beam oscillation samples were done in an IPG 1kW Fiber Laser machine. Both machines use a 1077 nm wavelength beam; the spot size of the Mundt and IPG are 0.012 and 0.002 inch respectively. Argon was coaxially flowed through the nozzle at 40 $\frac{L}{min}$ to act as shielding gas. Power checks for both machines were done with an Ophir power meter three times and averaged before each batch of welding; the demanded, measured, and power density values calculated from Equation 1 can be seen in Table 3 and 4.

$$P_\rho = \frac{P_{meas.}}{A_{beam}} \tag{1}$$

The first test matrix used both Inconel 625 and Ti-6Al-4V on either side of a vanadium interlayer. After fabrication of these samples it was decided that Ti-6Al-4V could be removed from the joint as there were no apparent issues in the weld metal between it and the vanadium. Subsequent fabricated samples then used Inconel 625 on both sides of a vanadium insert to maximize material usage. Multiple test matrices were completed based on the laser weld parameters shown in Table 5. Each matrix changed one parameter at time; for example we varied the laser power in the first, scan speed in the second, offset in the third, and combined offset and scan speed in the fourth.

Table 3: Mundt demanded power and average Ophir readout

Demanded power (W)	Ophir readout (W)	Power density $\left(\frac{kW}{cm^2}\right)$
475	384	526
575	491	673

Table 4: IPG demanded power and average Ophir readout

Demanded power (W)	Ophir readout (W)	Power density $\left(\frac{kW}{cm^2}\right)$
325	256	$126 \cdot 10^2$
450	404	$200 \cdot 10^2$

Table 5: Overview of parameters tested

Matrix #	1		2	3	4
Mode	CW	Wobble	CW	CW	CW
Power (W)	475, 575	325, 450	575	575	575
Scan speed (ipm)	80	80	100, 120, 140, 160	80	100, 120, 140, 160
Offset (thou)	0	0	0	3 & 4	3
Frequency (Hz)	∼	300	∼	∼	∼
Amplitude (in)	∼	0.024	∼	∼	∼

4.2.3 Preparation of Samples

After fabrication, samples were imaged with a Hirox KH-7700 digital microscope in the ”as-welded” condition. There were then pre-mounted in Buehler EpoThin 2 epoxy before processing. The samples were cut using a Buehler MetSaw equipped with a silicon carbide abrasive wheel under flood coolant. A cross-sectional cut was made at the halfway point of the weld length to analyze the steady state region. These cross-sections were then re-mounted in epoxy and metallographically ground with 120 and 600 grit SiC paper and polished with 9, 3, 1, 0.3, and 0.05 μm alpha alumina slurries.

4.3 Characterization

The microstructure was analyzed using an Olympus microscope, a JEOL IT700HR FE-SEM, and a Buehler MicroMet 6000 series indenter. The Vicker’s Microhardness was conducted on

100kgf and a 30 second dwell time. Wavelength Dispersive Spectroscopy (WDS) was done with four different detectors on a CAMECA SX100 Microprobe, one set to chromium and vanadium, and two on nickel. Energy Dispersive Spectroscopy (EDS) was completed on on some BSE solidification images to look at relative composition.

5 Results

5.1 Theoretical

An equilibrium phase diagram was calculated with 100% Inconel 625 varied to 100% vanadium through PanDAT's Nickel database. Scheil solidification diagrams were calculated in the same database at the 50/50, 60/40 and 40/60 Inconel 625 and vanadium weight percentages.

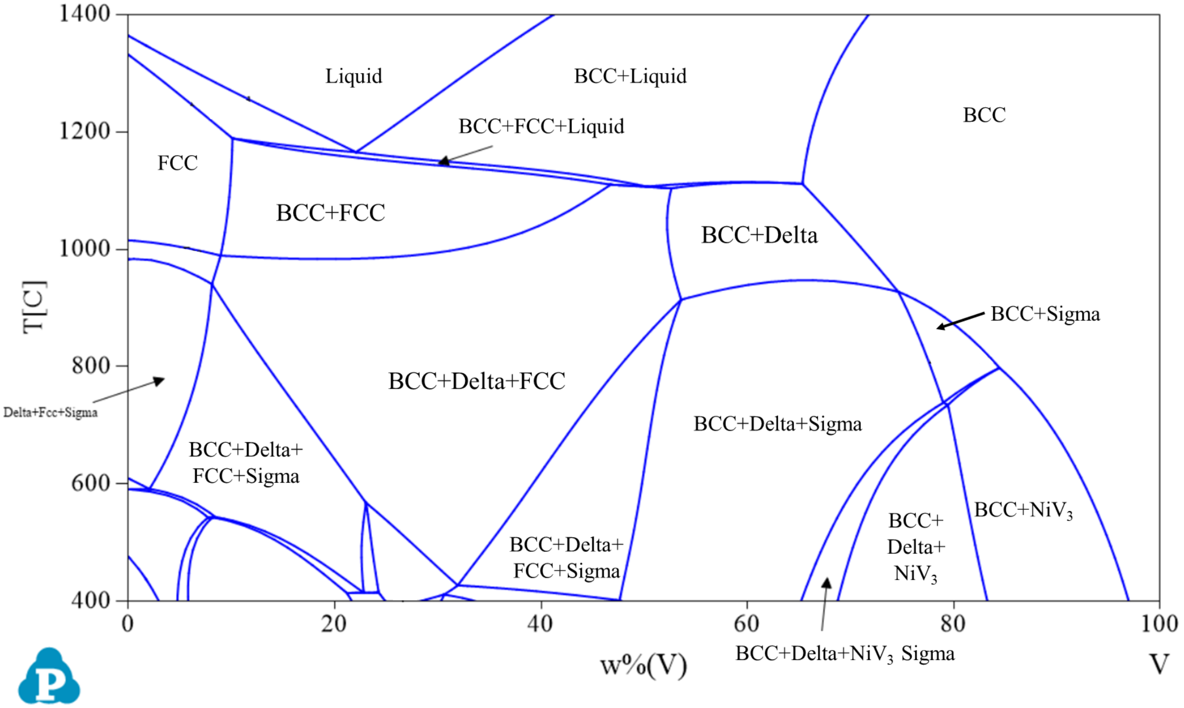

Figure 8: Inconel 625 and vanadium equilibrium phase diagram

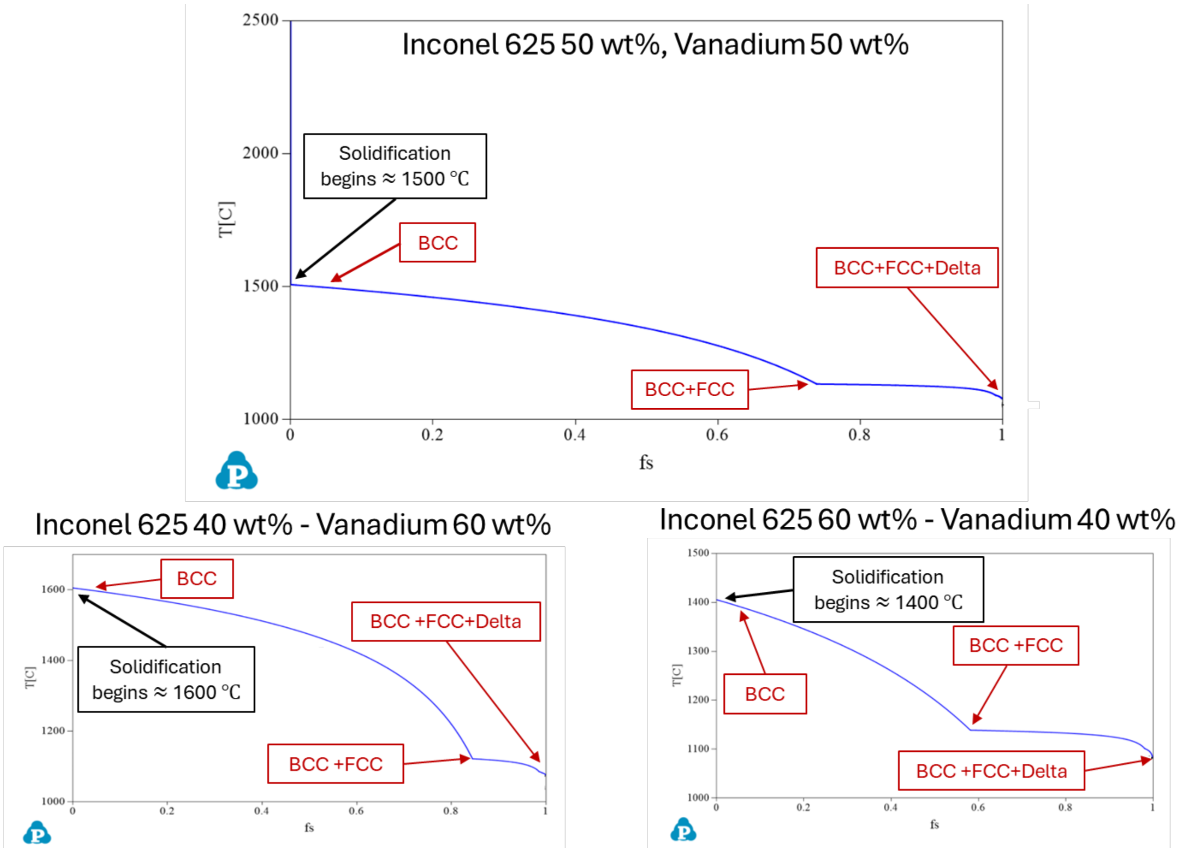

Figure 9: Scheil solidification diagrams

5.2 Weld Overviews

After fabrication, images were taken with the Hirox microscope in the as-welded condition to verify if the weld had cracked or was crack free. Top down overviews from all four matrices can be seen below:

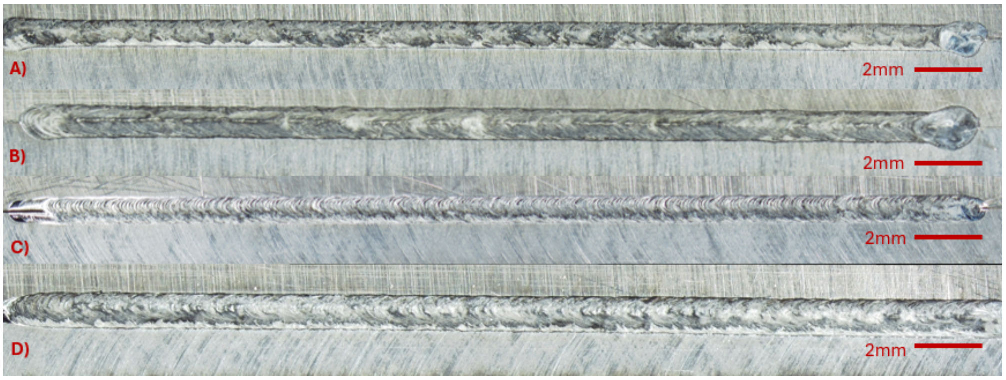

Figure 10: Matrix 1: A) 475W CW B) 575W CW C) 325W Wobble D)450W Wobble

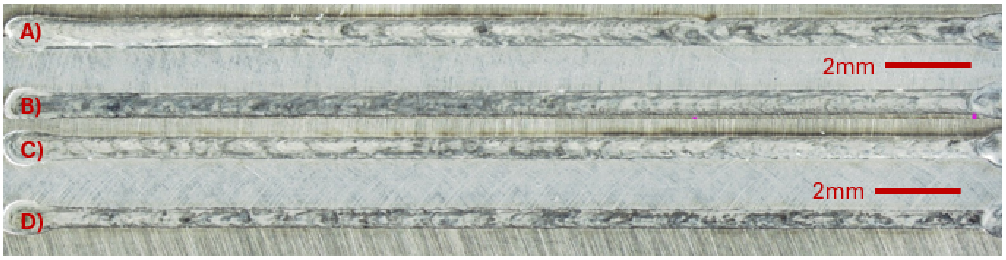

Figure 11: Matrix 2: A) 100 ipm CW B) 120 ipm C) 140 ipm D) 160 ipm

Figure 12: Matrix 3: A) 0.003" into Inconel 625 B) 0.003" into vanadium C) 0.004" into Inconel 625 D) 0.004" into vanadium

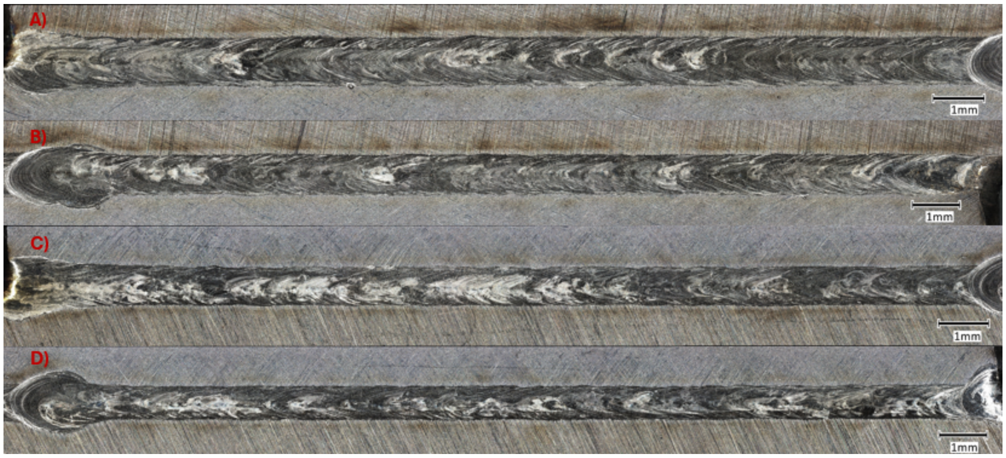

Figure 13: Matrix 4: A) 100 ipm B) 120 ipm C) 140 ipm D) 160 ipm

5.3 Weld Cross Sections

Side profiles were taken of each weld to view weld pool shape and behavior either optically or on the BSE - SEM detector.

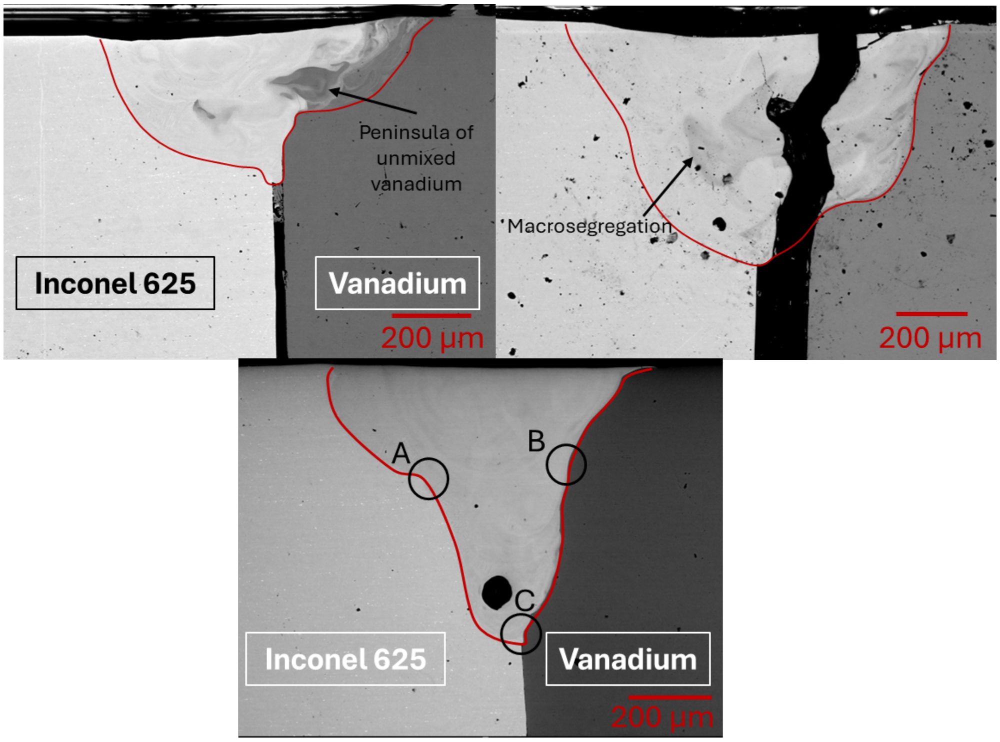

Figure 14: Matrix 1 Wobble Top Left: 325W Top Right: 450W Bottom: 575W Continuous Wave

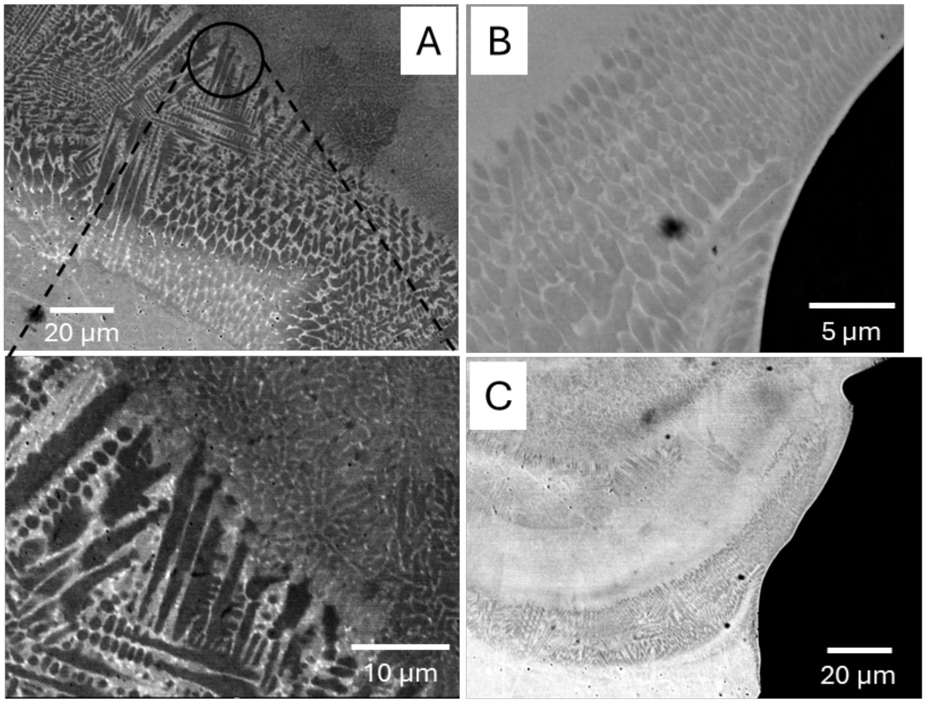

Figure 15: CW 575W Solidification Substructure

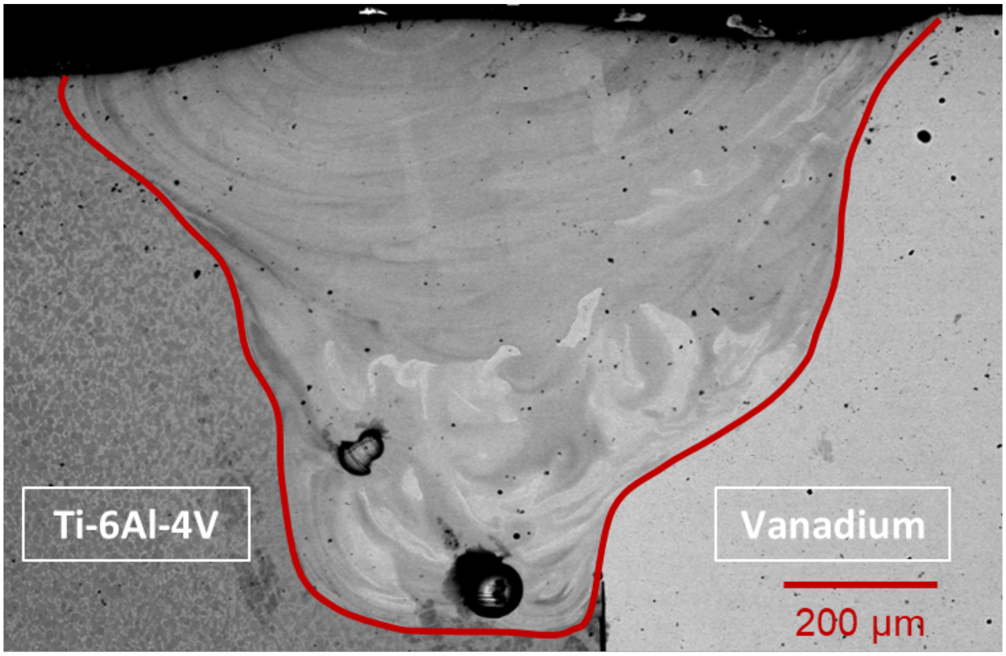

Figure 16: Wobble 450W Ti-V Weld

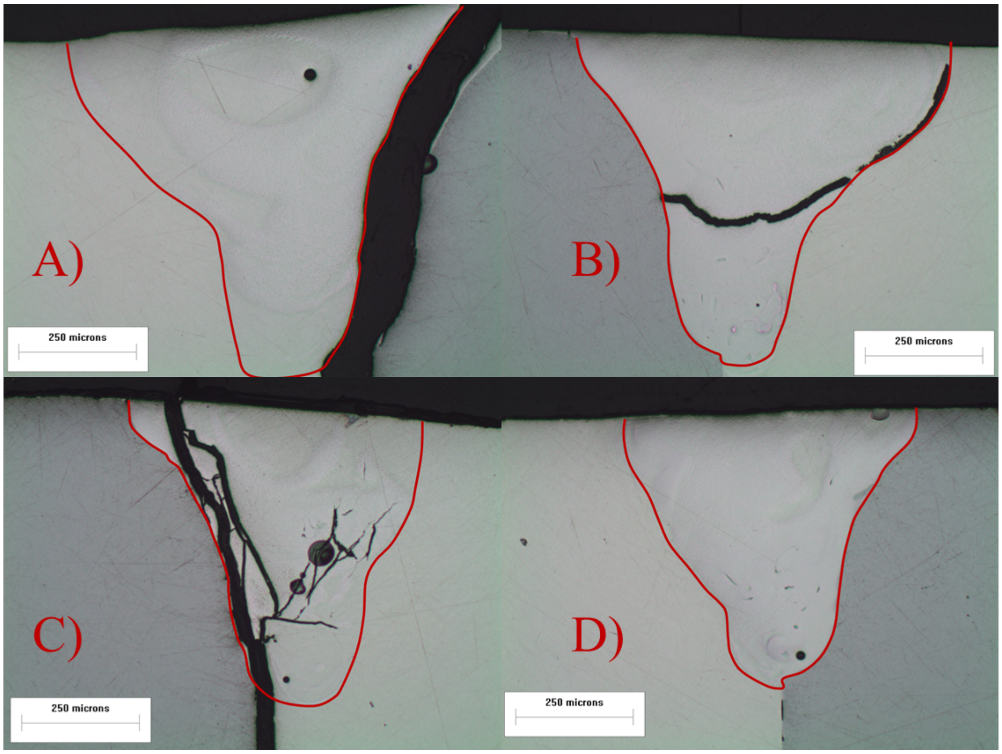

Figure 17: Matrix 2 A) 100 ipm B) 120 ipm C) 140 ipm D) 160 ipm

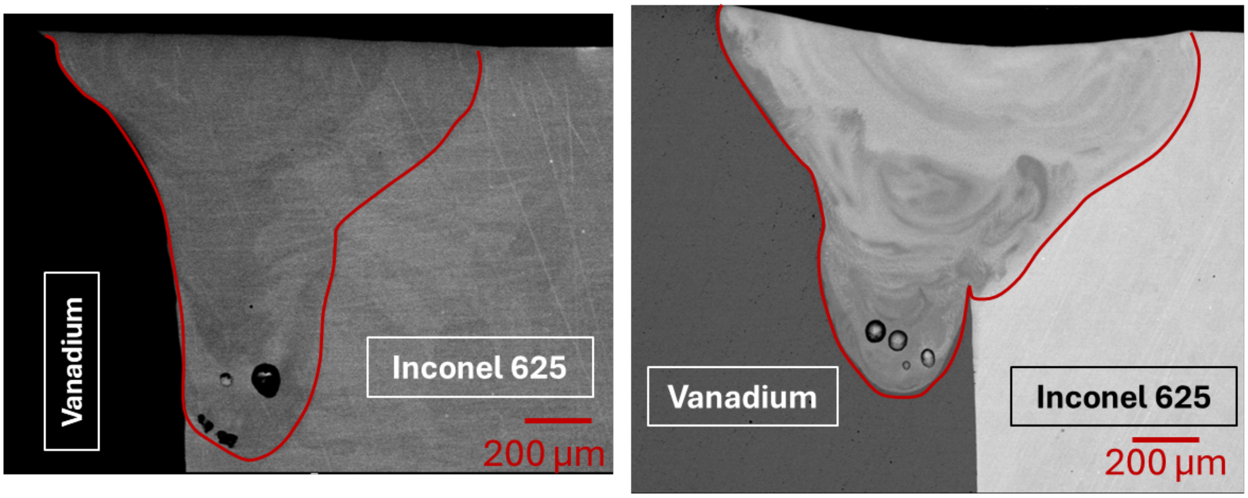

Figure 18: Matrix 3: (Left) 0.003” Inconel 625 Offset (Right) 0.004” vanadium Offset

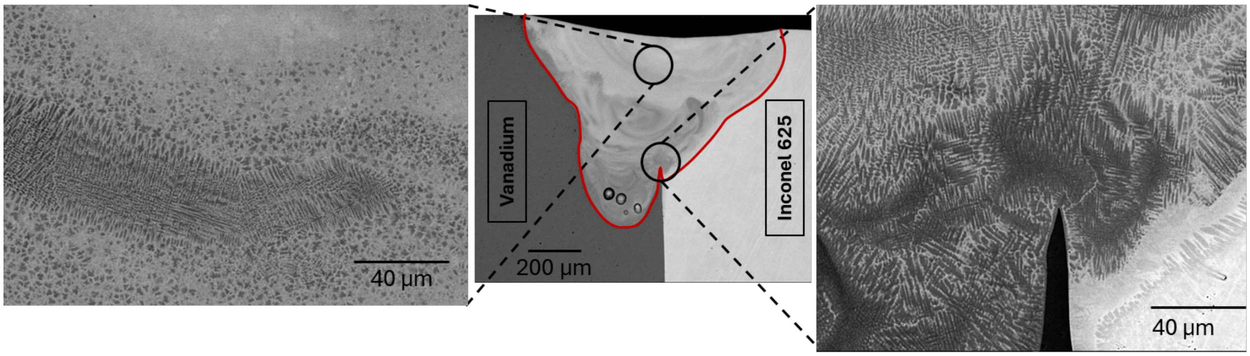

Figure 19: Matrix 3: BSE 0.004” into vanadium

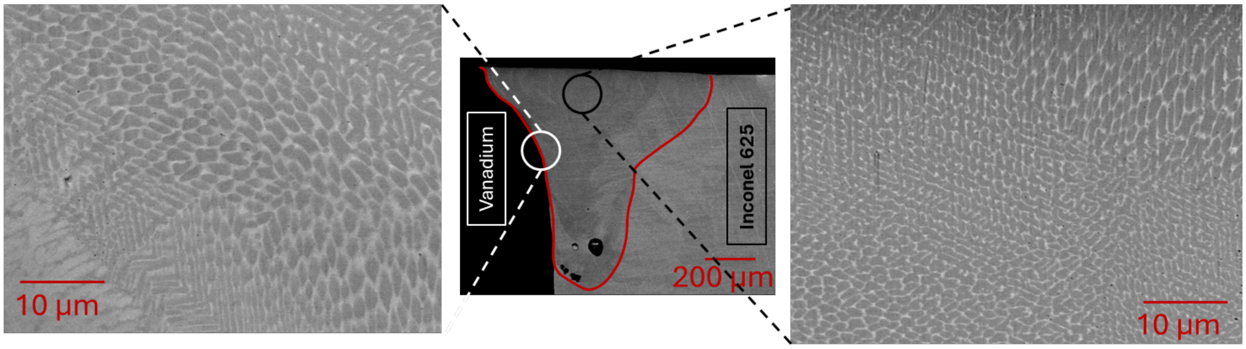

Figure 20: Matrix 3: BSE 0.003” into Inconel 625

Width and depth of each Inconel-vanadium weld from matrix 1 and 2 was measured in ImageJ.

Table 6: Matrix 1 weld measurements

Power	Scan Speed (ipm)	DOP (in)	Width (in)
Wobble 325W	80	0.016	0.032
Wobble 450W	”	0.030	0.044
CW 475W	”	0.019	0.034
CW 575W	”	0.029	0.038

Table 7: Matrix 2 weld measurements

Power	Scan Speed (ipm)	DOP (in)	Width (in)
CW 575W	100	0.029	0.037
”	120	0.028	0.033
”	140	0.025	0.027
”	160	0.023	0.026

5.4 Vickers Microhardness Data

Vickers Microhardness was done on each weld going across the top of the weld. Some samples had severe crack bifurcation and thus limited data points could be collected. Vickers hardness (VHN) plotted against distance from weld centerline are shown in the following plots:

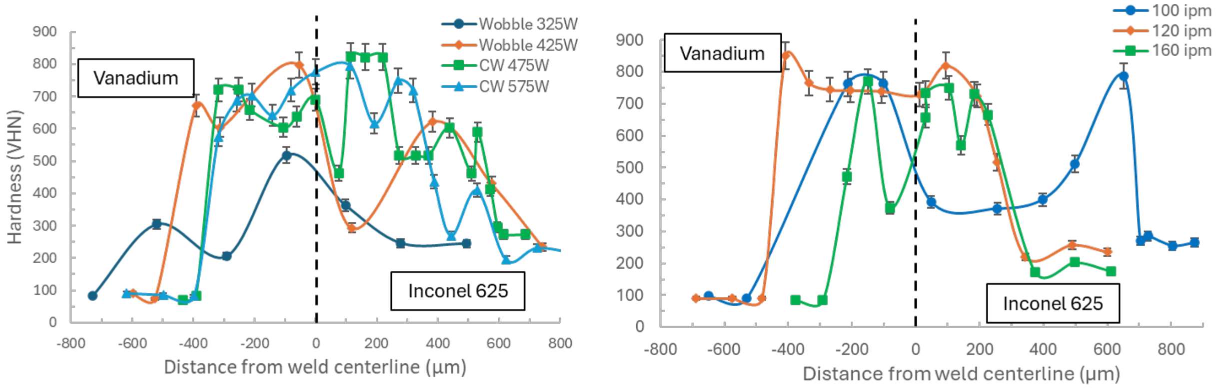

Figure 21: Matrix 1 & 2 Hardness plots

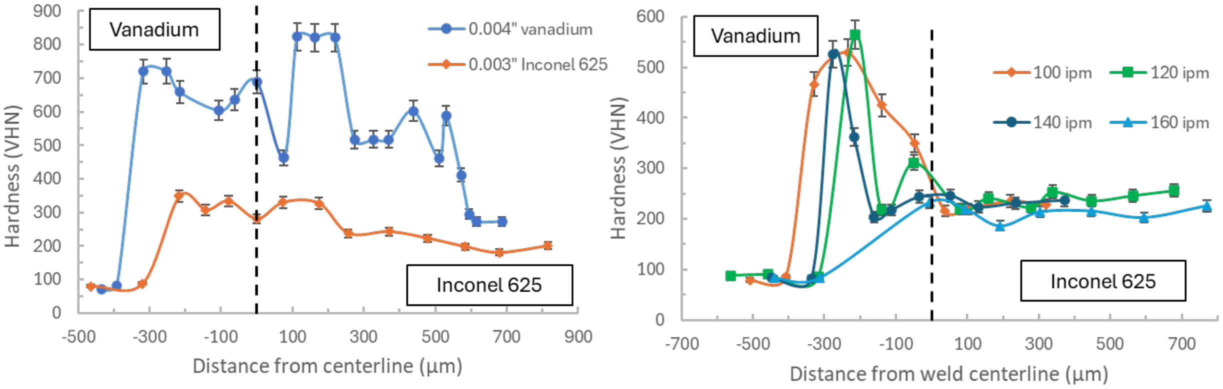

Figure 22: Matrix 3 & 4 Hardness plots

5.5 WDS & EDS

Wavelength Dispersive Spectroscopy (WDS) was completed on three samples, CW 575 (our baseline), 0.003” Inconel 625 offset, and 0.004” vanadium offset with line scans going horizontally and vertically across the weld.

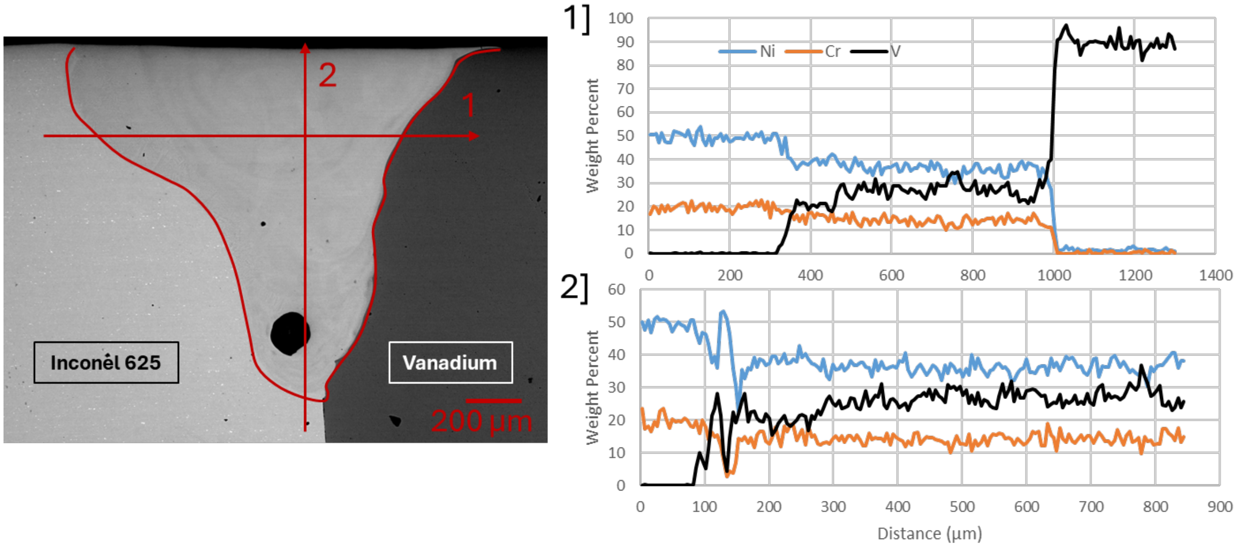

Figure 23: CW 575W

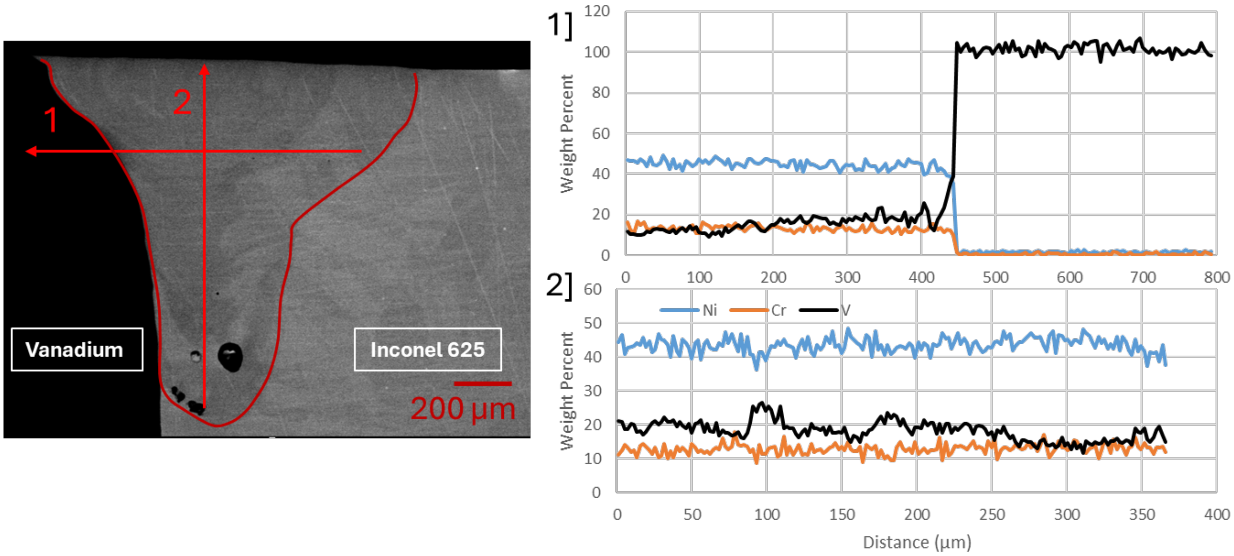

Figure 24: CW 575W 0.003” Inconel 625 Offset

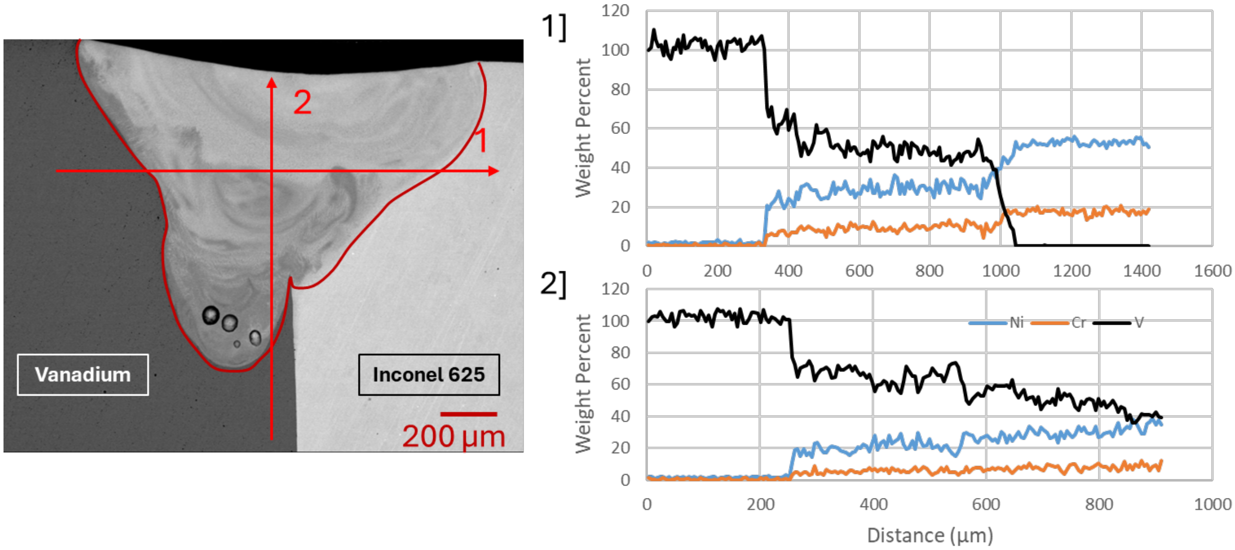

Figure 25: CW 575W 0.004” vanadium Offset

Energy Dispersive Spectroscopy (EDS) was done on the dendritic substructure to understand the microsegregation and compositional changes. The image and plot can be seen below:

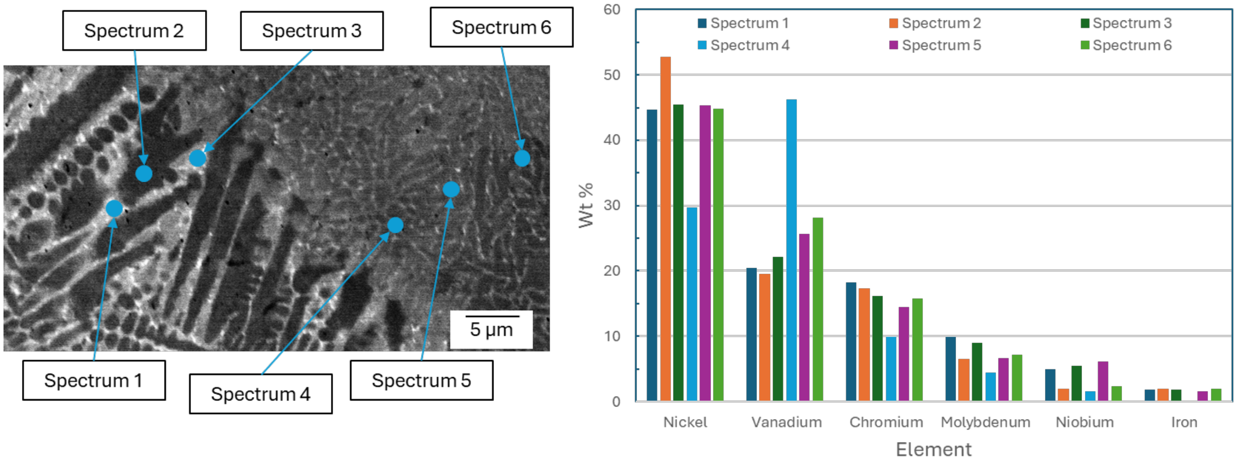

Figure 26: EDS Point Spectra of 575W CW Sample

6 Discussions

Transverse welds cracks were found in all samples from test matrices one, two and four as seen in Figures 10, 11, and 13. These cracks could be heard occurring as soon as the hutch to the machine was opened after welding. These cracks are sub-solidus cracks, it is important to make the distinction that these are not solidification cracks. In Matrix 3, there was qualitatively a larger amount of cracks in the vanadium offsets, and less in the Inconel 625 offsets as seen in Figure 12. In fact, no transverse cracks were observed in the 0.003" offset into the Inconel 625 sample's overview. It is also important to note the cracking observed in the micrographs such as Figure 17a & 17c happened during the cutting operation; it highlights the brittle nature of the welds. In Figure 17c, in particular, there are large amounts of crack bifurcation due to the extreme brittleness that occurred from cutting operation cracking.

There is asymmetrical behavior at the root of the weld due to vanadium melting at a higher temperature than Inconel 625 as seen in Figure 14. This effect seems to be more apparent with lower laser powers and in beam oscillation welds. In Figures 14 and 17, we see a decrease in the step like behavior in continuous wave welds.

Figure 14 also highlights the macrosegregation that occurs in the fusion zone. The peninsula depicted in Figure 14 is not uncommon to see in dissimilar-metal welding and also comes from the temperature of the melt pool being less than the melting point of the base material ($T_{lw} < T_{vanadium}$) [19]. The unmixed melted vanadium is dragged into the melt pool and fast frozen before having a chance to mix; this leaves peninsulas or even islands as shown. The continuous wave samples did not have the same amount of macrosegregation as wobble welds did; CW welds also contain less variables than wobble welds which is why it became the focus in matrices 2-4.

The propagation behavior of the solidification front depends on the $(\frac{G}{R})$ ratio where G is the temperature gradient and R is the growth rate. In a decreasing $(\frac{G}{R})$ ratio the solidification behavior changes from planar → cellular → dendritic → equiaxed dendritic.

The temperature gradient is a function of the amount of constitutional undercooling that is occurring in the liquid ahead of the solid/liquid interface; this is caused by solute rejection from the solid to the liquid. This is verified by Figure 26 where EDS point scans qualitatively show that the dendritic regions are richer in nickel and the interdendritic regions are richer in vanadium, molybdenum, and niobium.

Figure 15 is a collage of zoomed in micrographs that highlight how the macrosegregation effects the microsegregation and subsequent solidification substructure. In Figure 15a there is a sharp transition from columnar dendritic to planar growth that lines up with a band of vanadium rich weld metal (darker in BSE). Figure 15b shows the other side of the joint where the substructure is cellular. Figure 15c is a zoomed in micrograph of the weld root where the bands of columnar dendritic and planar substructure are apparent.

Figures 19 and 20 show that the solidification substructure changes drastically as a function of vanadium content in the weld metal. The micrographs in Figure 19 show the columnar dendritic nature at the root of the weld and in the band of vanadium towards the top of the weld. Moving towards the weld centerline the substructure changes from columnar dendritic to equiaxed dendritic because the growth rate of the front essentially becomes the welding speed $R = \nu$. The micrographs in Figure 20 show that the substructure is primarily cellular which may be an underlying reason on why that weld didn't show sub-solidus cracks; with less undercooling there may be less solute being rejected into the interdendritic region which may in turn limit the intermetallic formation.

In Figure 16, there is the Ti-6Al-4V and Vanadium weld showcased with no transverse or solidification cracks. This is because vanadium is fully soluble in $\beta-$Ti as seen in the binary phase diagram from the ASM Handbook Vol. 3 in the Appendix.

In Figure 18, there is minimal changes in terms of composition from the weld pool and Inconel 625. The vanadium base metal had to be blacked out during BSE imaging to get the weld profile to resolve. Comparing this to the 0.004" offset into the vanadium there is a stark contrast in weld pool behavior due to less mixing.

There was no noticeable difference in depth and width between the two types of laser welded in this study as seen in Table 6. In Table 7, we notice a decreasing width and depth trend as we increase our scan speed because the beam is spending less time per unit area to melt the material.

The idea behind increasing the scan speed for test matrix two was that we could reduce the amount of intermetallic formation by increasing the effective cooling rate. Laser welding cooling rates are on the order of $10^3 \frac{°C}{sec}$ so we are already a long ways from equilibrium. The increased scan speed actually may have increased the crack susceptibility of the weld as there is more thermal strain associated with the higher scan speeds; this can be seen in Figure 17. There is preferential cracking along the vanadium side of the joint which could be a function of the higher chromium and vanadium content on that side. That side of the joint would have decreased ductility when compared to the Inconel side with it's FCC crystal structure. It is important to note that although it looks like Figure 17d is crack free it is not. Figure 17c shows crack bifurcation that highlight the increased strain energy from the increased cooling rate.

The third matrix focused on offsetting the beam to the either the Inconel or vanadium side to observe the effect on the microstructure. By offsetting the beam we are effectively melting less of one of the two materials; this would shift us either left or right in our calculated phase diagram shown in Figure 8. The samples that were offset into the vanadium by 0.003 and 0.004 inches cracked the worst out of any sample fabricated during this project. This is likely due to having more of the BCC (less ductile) crystal structure making up the weld metal along with the possible formation of brittle sigma and NiV_3 phases. The 0.004 inch offset into the Inconel 625 also had transverse weld cracks although less than any of the previous weld fabricated. The 0.003 inch offset did not show transverse cracks after careful observation of the overview images. After metallographic preparation, the sample still did not show cracking unalike the other samples did after processing. It also did not crack during Vickers microhardness. Despite the results coming back that it is in fact a sound weld it would be worth while to fabricate it again under the same conditions to validate repeatability. The fact that the 0.004 inch offset did crack may outline the small process window that exists for this joint.

The last test matrix looked at the effect of offset into the Inconel and scan speed together. All the samples from this batch showed transverse cracks. Although there may be less vanadium in the weld metal this was outweighed by the increased thermal strains associated with the higher cooling rates.

Looking at the Vickers Microhardness plots in Figures 21 and 22, there is a lot of inconsistency occurring between across the weld. This is due to the macrosegregation as seen in Figures 14, 16, and 18 for example. In Figure 16 we can visibly see the relief due to the spots in the weld that are harder versus not. Vanadium has a VHN of approximately 70 and Inconel 625 is approximately 250, but the weld pool reaches 700-800 in a lot of the cracked samples. There is also this large jump from the vanadium to weld pool side indicating there is a lot of intermetallics forming in that area of the weld while the Inconel side of the weld has a more gradual transition. In Figure 22, 0.003" Inconel 625 offset has a peak hardness around 350 VHN and a more consistent and gradual transition across the weld pool. This is due to a decrease in intermetallic formation. This decrease in hardness also corresponds to Figure 18 where we are unable to see a lot of macrosegregation in the 0.003" Inconel 625 offset sample. In Matrix 4, in Figure 22, we see a sharp peak on the vanadium side of the weld pool, but it quickly drops off. This is due to there being less vanadium melted and mixed into the weld as the scan speed is increased with the Inconel 625 offset.

The WDS results as seen in Figures 23-25 show how compositionally there is macrosegregation in the weld. In our baseline weld, 575W CW, across the weld there is rough 30 wt% vanadium and then a sharp increase at the interface between the weld pool and vanadium. Traveling up the weld vertically, there is macrosegregation based on the peaks but it is consistent in there roughly being 35-40 wt% Nickel content. It is important to note that these welds do not necessarily add up to 100 wt% due to only being able to detect 3 elements at one time on the microprobe.

In Figure 24, despite the line scan not starting in the pure Inconel 625, there is a gradual increase going from 10 wt% to 20 wt% across the 0.003" weld pool, and then there is the sudden jump to 100 wt% vanadium. In Figure 25, there is not as stark of a jump but across the weld there is around 50 wt% vanadium. In the vertical line scan there is a noticeable decrease in the vanadium due to the fast freezing of the vanadium with its higher solidification temperature than Inconel 625.

7 Conclusions

Utilizing vanadium as a single element interlayer to join Inconel 625 and Ti-6Al-4V through laser beam welding was explored both theoretically and experimentally. Theoretically vanadium performed the best out of other refractory metals in PanDat CALPHAD calculations of equilibrium phase diagrams and Scheil solidification diagrams. It was seen that in the joint between Inconel 625 and vanadium the FCC formation increased with decreasing vanadium content and that during solidification the only intermetallic formed was a tiny amount of δ phase at terminal solidification. Experimentally, the welds between vanadium and Ti-6Al-4V were well behaved and showed no cracking as theorized and seen in previous research. On the Inconel 625 and vanadium side of the joint all but one weld showed sub-solidus transverse cracks due to longitudinal shrinkage strain and intermetallic formation. Increasing the effective cooling rate through scan speed led to a smaller weld and increased crack density, offsetting into the vanadium led to increased crack density, and offsetting into the Inconel 625 0.003 inches led to a crack free joint.

The weld that didn't show cracking may not be intermetallic free but the lower and more consistent hardness values verify that there is less present when compared to other samples. Combining scan speed with offset into Inconel 625 didn't show a similar outcome as it did with Chen[18]; all welds from this matrix showed transverse cracks from intermetallic formation verified by large Vickers microhardness values along the vanadium side of the weld. The combination of increased cooling rate from scan speed and limited mixing from the offset increased the crack susceptibility of the joint. BSE images illustrated how the macrosegregation effects the microsegregation and the subsequent solidification substructure. There was a sharp change from columnar dendritic to planar when the weld metal moved from nickel rich to vanadium rich. We also saw that offsetting the beam into the vanadium produced a heavily dendritic substructure and offsetting into the Inconel produced a cellular substructure. EDS data also proved that on the Inconel 625 side of the weld metal the higher Z (molybdenum, niobium, vanadium) solute atoms were ejected from the growing dendrites into the interdendritic region which agrees with our Scheil solidification prediction. WDS was used to examine the effect of offset on the weld composition where the crack free weld had a vanadium content ≤ 20 wt%.

8 Acknowledgments

We would like to acknowledge and thank Sandia National Laboratories and New Mexico Institute of Mining and Technology Materials and Metallurgical Engineering Department for their help and resources during this project.

9 Conflict of Interest statement

The authors declare that there is no conflict of interest regarding this paper.

10 References

1. Allison, A. (n.d.). Prepared by the Joining Sub-Platform 2014. Retrieved April 6, 2025, from http://www.joining-platform.com/documents/Joining%20Sub-Platform%20SRA%20-%202014.pdf

2. Hanson, K. (2019, October 28). Traditional Versus Laser Welding. Advanced Manufacturing. https://www.advancedmanufacturing.org/manufacturing-engineering/traditional-versus-laser-welding/article_eebebcaa-e452-11ee-ba88-d7545b7e50d3.html

3. Wittemer, M., Grünewald, J., Wudy, K. (2023). Absorbance measurement for in situ process regime identification in laser processing. The International Journal of Advanced Manufacturing Technology, 126(1-2), 103–115. https://doi.org/10.1007/s00170-023-11041-9

4. Phillips, D. H. (2015). Welding Engineering. John Wiley Sons.

5. Mukherjee, T., Gao, M., Palmer, T., T. DebRoy. (2023). Keyhole mode wobble laser welding of a nickel base superalloy - Modeling, experiments, and process maps. Journal of Manufacturing Processes, 106, 465–479. https://doi.org/10.1016/j.jmapro.2023.10.017

6. Schematic Diagram of Laser Welding Setup, www.researchgate.net/figure/Schematic-diagram-of-laser-welding-setup fig1 327078452. Accessed 26 Sept. 2024

7. Corigliano, P. (2021). Non-linear finite element analysis of a Ti6Al4V/Inconel 625 joint obtained by explosion welding for sub-sea applications. Underwater Technology, 38(1), 13–16. https://doi.org/10.3723/ut.38.013

8. Sumeet Kabburi, shinde, H. (2025). Effect Of Different Turbine Blade Materials On The Performance Of Jet Engine Turbine. INTERNATIONAL JOURNAL of CREATIVE RESEARCH THOUGHTS, 13(1), c1–c36. https://doi.org/10.1729/Journal.43089

9. “Welding Difficult and Dissimilar Metals — EB Industries.” Https://Ebindustries.com/, ebindustries.com/welding-difficult-and-dissimilar-metals/.

10. Wenbo Wang a, et al. “Laser Melting Deposition of INCONEL625 to Ti6al4v Bimetallic Structure via Vanadium Interlayer.” Optics & Laser Technology, Elsevier, 14 Jan. 2024,

11. Liu, Jing, et al. “Microstructure and Mechanical Properties of Laser Welding of TI6AL4V to Inconel 718 Using Nb/Cu Interlayer.” Journal of Materials Processing Technology, Elsevier, 31 Oct. 2019,

    www.sciencedirect.com/science/article/pii/S0924013619304406.

12. T, Junaid M, Khan FN, Akbar UA, Saeed Hakeem A. Dissimilar tungsten inert gas welding between Inconel 718 and commercially pure titanium using a vanadium interlayer. Proceedings of the Institution of Mechanical Engineers, Part L: Journal of Materials: Design and Applications. 2022;236(4):715-729. doi:10.1177/14644207211054265

13. Hu, Yungfeng, et al. “Fiber Laser Welding of Ti–6al–4v to Inconel 718 Bimetallic Structure via Cu/Ta Multi-Interlayer.” ScienceDirect, Vacuum, 20 July 2021, www.sciencedirect.com/science/article/pii/S0042207X21004115.

14. Yan, Li, et al. “Effect of Laser Welding Parameters on the Temperature Distribution, Microstructure and Mechanical Properties of Dissimilar Weld Joint of Inconel 625 and Stainless Steel 304.” International Communications in Heat and Mass Transfer, vol. 131, Feb. 2022, p. 105859, https://doi.org/10.1016/j.icheatmasstransfer.2021.105859. Accessed 18 Apr. 2022.

15. H. Ramezani, S.A.A. Akbari Mousavi, H. Ebrahimzadeh The effect of process parameters on pulsed Nd:YAG laser welding of Inconel 625 Adv. Mater. Res., 829 (2014), pp. 36-40

16. Akman, E., et al. “Laser Welding of Ti6Al4V Titanium Alloys.” Journal of Materials Processing Technology, vol. 209, no. 8, Apr. 2009, pp. 3705–3713, www.sciencedirect.com/science/article/pii/S0924013608006572, https://doi.org/10.1016/j.jmatprotec.2008.08.026.

17. Nickel alloy 625, inconel® 625. (2023, August 8). Continental Steel & Tube Company. https://continentalsteel.com/nickel-alloys/grades/inconel-625/

18. Chen, H.-C., Pinkerton, A. J., Li, L. (2010). Fibre laser welding of dissimilar alloys of Ti-6Al-4V and Inconel 718 for aerospace applications. The International Journal of Advanced Manufacturing Technology, 52(9-12), 977–987. https://doi.org/10.1007/s00170-010-2791-3

19. Sindo Kou. (2020). Welding Metallurgy. John Wiley.

20. Zapirain, F., Zubiri, F., Garciandía, F., Tolosa, I., Chueca, S., Goiria, A. (2011). Development of Laser Welding of Ni based Superalloys for Aeronautic Engine Applications (Experimental Process and Obtained Properties). Physics Procedia, 12, 105–112. https://doi.org/10.1016/j.phpro.2011.03.014

11 Appendix A

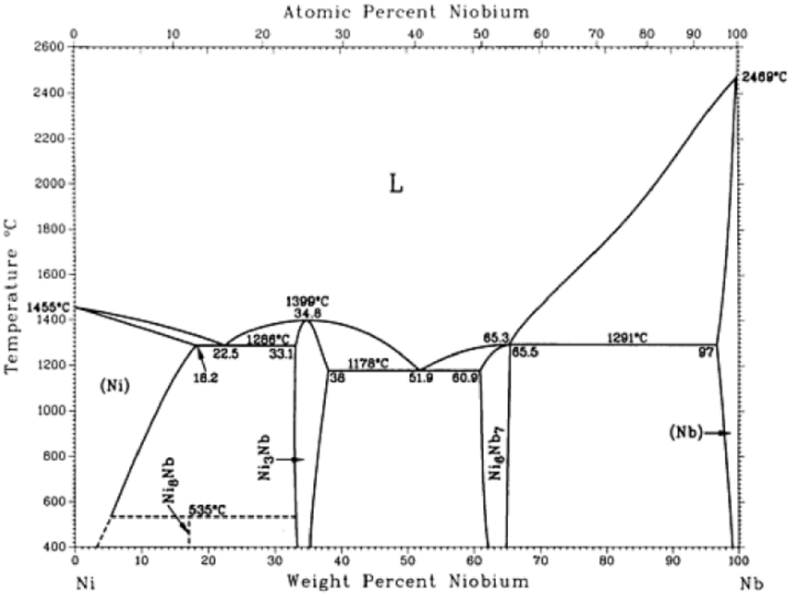

Figure 27: Nb-Ni phase diagram [H. Okamoto, 1992]

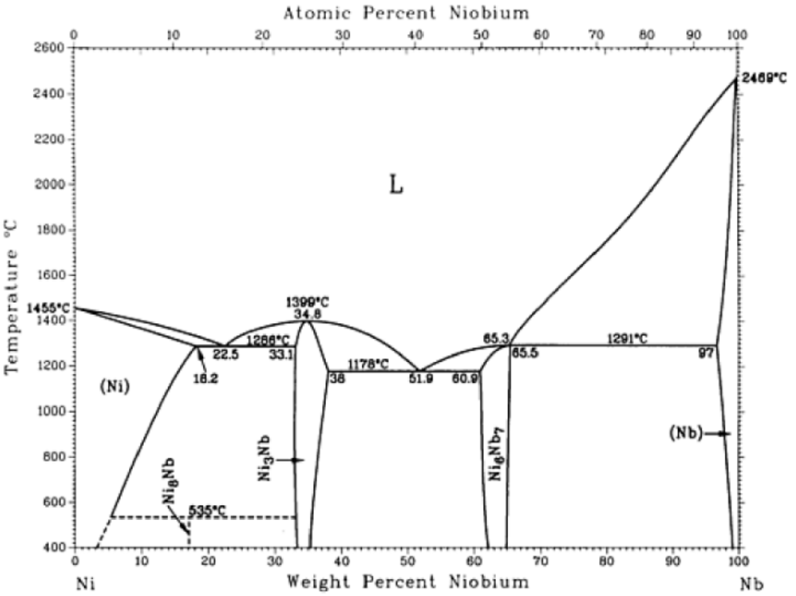

Figure 28: Ni-Mo phase diagram [H. Okamoto, 1991]

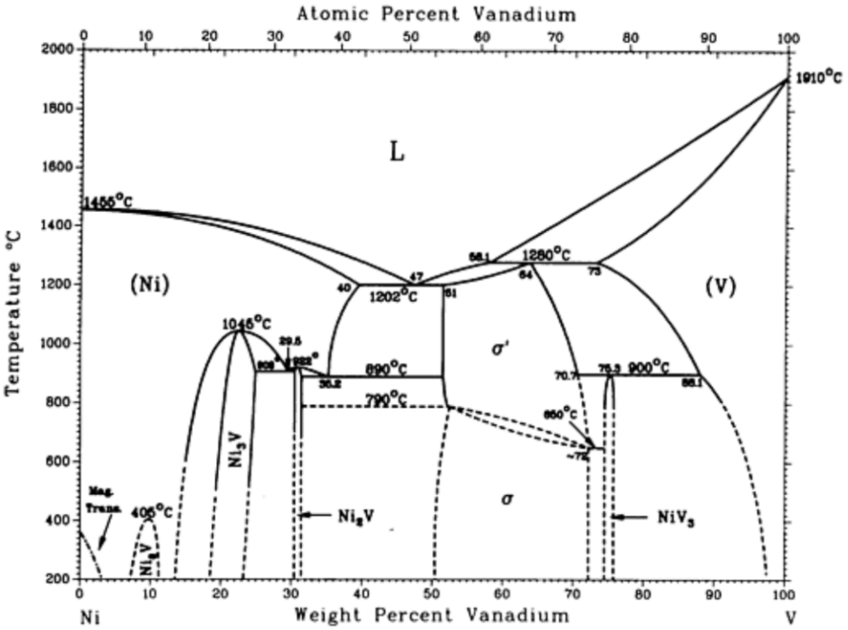

Figure 29: Ni-V phase diagram [J.F. Smith, O.N. Carlson, and P. Nash, 1991]

Table 8: Inconel 625 composition[17]

Element	Ni	Cr	Mo	Fe	Nb
Wt %	58 min	23	10	5	4

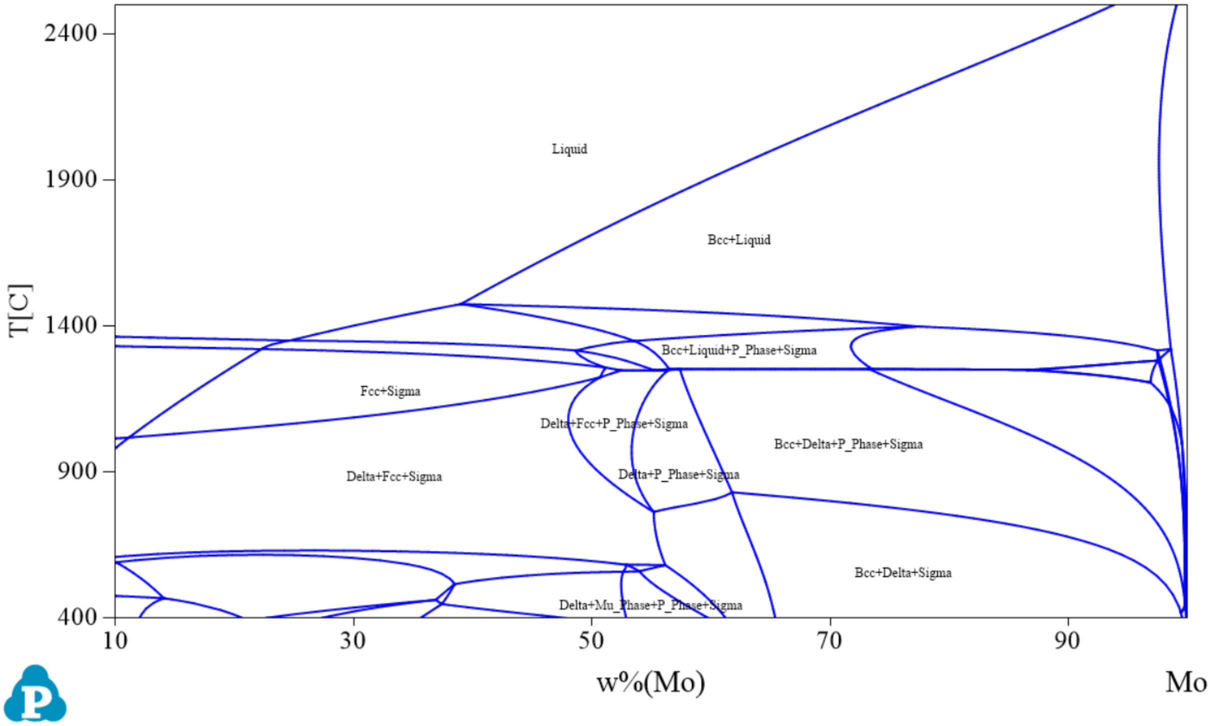

Figure 30: Inconel 625 - Molybdenum phase diagram

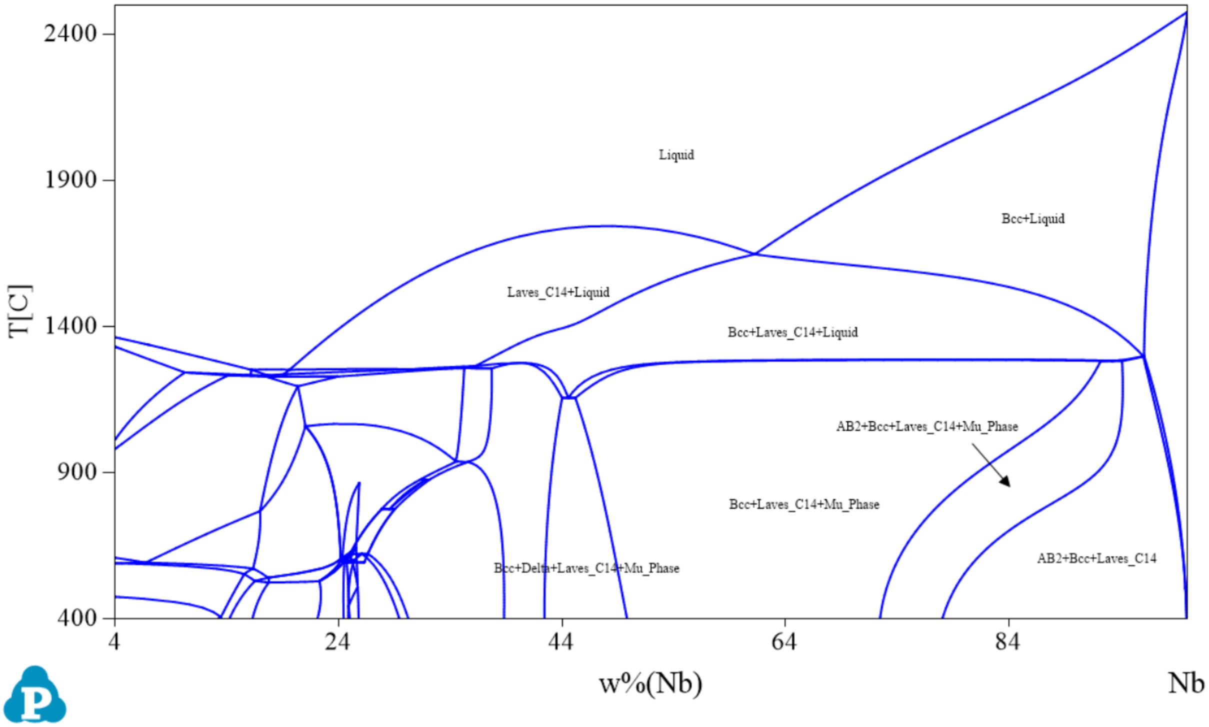

Figure 31: Inconel 625 - Niobium phase diagram

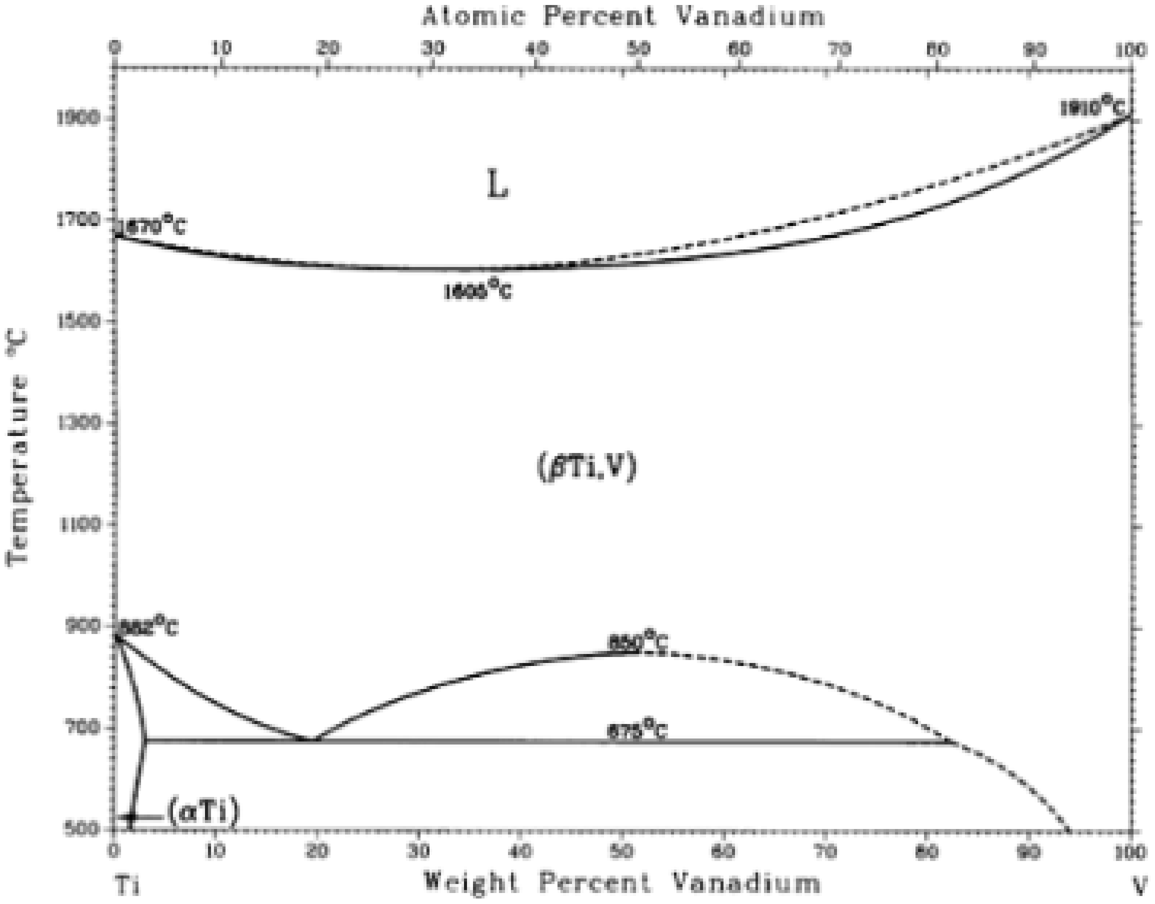

Figure 32: Vanadium Titanium Binary Phase Diagram